Applied Physics A (2026) 132:409
https://doi.org/10.1007/s00339-026-09460-y

Applied Physics A
Materials Science & Processing

REGULAR PAPERS

Tailored MoO_3 hole transport layer for performance enhancement in lead-free hybrid tandem perovskite solar cell

Zulfanizam Abdul Wahab[1] · Nabilah Ahmad Jalaludin[1] · Nur Aliesa Johari[2] · Ahmad Nizamuddin Mustafa[1,3] · Mazlin Aida Mohamood[4] · Fauziyah Salehuddin[1] · Mohammad Aminul Islam[5] · Faiz Arith[1]

Received: 31 October 2025 / Accepted: 21 February 2026

Abstract
This study reports the design and optimization of a two-terminal tandem solar cell combining a lead-free perovskite top cell based on methylammonium tin iodide ($MASnI_3$) with a silicon bottom cell. Molybdenum trioxide (MoO_3) serves as the hole transport layer (HTL) in the perovskite cell, providing favorable energy alignment and chemical stability for efficient charge extraction. Careful passivation of interfacial defects at the MoO_3/$MASnI_3$ interface minimized non-radiative recombination and enhanced hole transport. The optimized perovskite sub-cell achieved a power conversion efficiency (PCE) of 20.48%, while the silicon bottom cell reached 15.72%, resulting in a tandem PCE of 34.19%. These results underscore the critical role of interfacial defect control and inorganic HTL engineering in improving lead-free perovskite/silicon tandem performance. This tandem architecture offers a promising route toward scalable, environmentally friendly photovoltaic devices surpassing single-junction efficiency limits.

Keywords Hole transport layer · Perovskite solar cell · Tandem Perovskite solar cell

1 Introduction

Recent advancements in photovoltaic (PV) technology have positioned it as a leading solution in the global shift toward sustainable energy. Increasing energy demand, rising fossil fuel costs, and the urgent need to reduce greenhouse gas emissions have accelerated the deployment of PV systems across various scales. Modern PV technologies offer significant environmental benefits, including minimal operational emissions and a substantially reduced life-cycle carbon footprint compared to conventional fossil-based energy sources. Their scalability from residential rooftop panels to utility-scale solar farms enables broad accessibility, particularly in remote and off-grid regions [1].

Within the PV landscape, perovskite solar cells (PSCs) have gained substantial attention as promising candidates for next-generation solar technologies. Their appeal lies in high power conversion efficiencies, low-cost solution-based fabrication, and tunable optoelectronic properties. A standard PSC structure consists of six functional layers: a glass substrate, a transparent conductive electrode, an electron transport layer (ETL), a perovskite absorber, a hole transport layer (HTL), and a metal back contact. The bandgap tunability of perovskite materials also enables the development of tandem architectures, offering a pathway to surpass the efficiency limits of traditional single-junction solar cells. These features collectively make PSCs a strong contender for scalable, efficient, and sustainable photovoltaic solutions [1].

Recent advancements in photovoltaic technology have concentrated on addressing the efficiency limitations of

✉ Faiz Arith
faiz.arith@utem.edu.my

1 Faculty of Electronic and Computer Technology and Engineering, Universiti Teknikal Malaysia Melaka, Hang Tuah Jaya, Durian Tunggal 76100, Malaysia

2 Department of Electrical and Computer Engineering, Seoul National University, 1 Gwanak-ro, Gwanak-gu, Seoul 08826, South Korea

3 Department of Materials, Faculty of Engineering, Imperial College London, London SW7 2AZ, UK

4 Smart Manufacturing Technology Centre (SMTC), Universiti Teknikal Malaysia Melaka, Hang Tuah Jaya, 76100 Durian Tunggal, Malaysia

5 Department of Electrical Engineering, Faculty of Engineering, University of Malaya, Kuala Lumpur 50603, Malaysia

Published online: 16 April 2026

single-junction solar cells through the development of tandem solar cells. These devices contain multiple sub-cells with differing bandgaps, arranged in a stacked configuration to capture various parts of the solar spectrum, thereby enhancing energy absorption and power conversion efficiency (PCE). Tandem solar cells can be fabricated in a two-terminal (2T), three-terminal (3T), or four-terminal (4T) configuration, each offering distinct benefits in terms of fabrication complexity and power management [2–5]. Tandem solar cells, particularly those combining perovskite absorbers with silicon, have attracted widespread attention due to their high efficiency and environmentally friendly properties. In these devices, the top cell primarily captures high-energy (short-wavelength) photons, allowing lower-energy (long-wavelength) photons to pass through to the bottom sub-cell, thereby maximizing overall light absorption and energy conversion [6]. The overall performance of tandem perovskite solar cells (TPSCs) is highly influenced by the properties and effectiveness of the hole transport layer (HTL). Among various materials explored, molybdenum oxide (MoO_3) has gained considerable attention as a superior HTL candidate due to its intrinsically high work function, exceptional hole mobility, and robust chemical and thermal stability. These characteristics facilitate efficient extraction and transport of photogenerated holes, thereby minimizing recombination losses and improving charge carrier dynamics within the device.

In particular, the integration of MoO_3 as the HTL in lead-free tandem perovskite solar cells has demonstrated significant enhancements in power conversion efficiency (PCE). This improvement arises not only from MoO_3's ability to optimize charge transport at the perovskite/HTL interface but also from its role in improving light management within the device. By promoting better energy level alignment and reducing interfacial defects, MoO_3 enables more effective light absorption and charge separation, which are crucial for achieving higher photovoltaic performance. Consequently, MoO_3-based HTLs contribute to both the stability and efficiency of lead-free TPSCs, positioning this material as a key component in advancing environmentally friendly, high-efficiency solar technologies [7]. Incorporating MoO_3 into tandem perovskite solar cell (TPSC) architectures significantly improves charge extraction, reduces recombination losses, and enhances both device efficiency and operational stability. Ukai R. et al. demonstrated that solution-processed MoO_3 combined with indium zinc oxide (IZO) interconnects in perovskite/silicon tandem cells effectively suppress recombination and facilitates efficient charge transport, resulting in power conversion efficiencies (PCEs) of approximately 18–19% [8]. The characteristics of MoO_3, including stability, low cost, and ease of production, render it a compelling choice for high-efficiency and stable perovskite solar cells (PSCs) [9]. This study introduces a novel molybdenum trioxide (MoO_3) based hole transport layer (HTL) configuration tailored for lead-free perovskite/silicon tandem solar cells. Although MoO_3 has been recognized for its high work function, strong chemical stability, and efficient hole extraction, its application in lead-free tandem devices remains limited. Here, MoO_3 is engineered to achieve effective band alignment and improved carrier selectivity through an integrated defect passivation approach. This mechanism, involving Mo–O–Sn bonding at the perovskite interface, minimizes interfacial recombination losses and enhances charge transport efficiency. Using SCAPS-1D simulation, the effects of HTL thickness, doping concentration, and interface defect density were systematically optimized to evaluate their impact on photovoltaic performance. The optimized structure achieved a simulated power conversion efficiency (PCE) of 34.19%, exceeding most reported experimental values for lead-free tandem architectures. These findings highlight the importance of interfacial defect management and inorganic HTL engineering in realizing high-efficiency, stable, and environmentally sustainable perovskite/silicon tandem solar cells.

C_{60} was selected as the electron transport layer (ETL) owing to its high electron mobility, deep LUMO level that enables selective electron extraction, and chemical stability at the perovskite interface [10]. Sublimed C_{60} has been shown to provide reproducible transport characteristics and to minimize interfacial recombination compared to oxide ETLs such as TiO_2 or ZnO, which often suffer from photocatalytic activity and interface instability under UV illumination [11]. Furthermore, recent approaches such as ionic salt-modified C_{60} have demonstrated enhanced charge transport and improved stability in inverted perovskite modules, reinforcing its suitability for tin-based perovskite systems [12]. These attributes make C_{60} a robust choice for achieving efficient carrier extraction and stable device operation in tandem architectures.

$MASnI_3$ was chosen as the absorber due to its lead-free composition and direct bandgap of approximately 1.3 eV, which is spectrally complementary to crystalline silicon in a two-terminal tandem configuration [13]. This bandgap enables efficient current matching with the silicon bottom cell, a critical requirement for 2 T tandems. Numerical and experimental studies have confirmed $MASnI_3$'s optoelectronic potential despite challenges such as Sn^{2+} oxidation, which can be mitigated through interface engineering and defect passivation [14] Compared to alternative absorbers such as mixed tin-germanium perovskites or double perovskites, $MASnI_3$ remains the most widely studied lead-free perovskite with validated performance in tandem architectures. The C_{60}/$MASnI_3$ combination therefore provides robust transport selectivity, spectral complementarity,

and compatibility with recent advances in stabilizing tin perovskites [10–14] (Fig. 1).

2 Tandem structure and simulation methodology

2.1 Tandem solar cell architecture and energy band alignment

All simulations in this study were conducted on a two-terminal (2T) monolithic perovskite/silicon tandem architecture. The four-terminal (4T) schematic shown in the introduction was included solely for conceptual contrast and is not part of the simulated model. Section 2.1 and Fig. 2(a) have been revised to present the complete 2 T stack, with captions updated to explicitly state the 2 T configuration. These revisions ensure consistency across the abstract, figures, and results, thereby removing any ambiguity [15–17]. The emphasis on the two-terminal (2T) architecture is consistent with recent reviews that highlight its efficiency, scalability, and industrial relevance[18], while drawing attention to critical aspects such as current matching and interface design. These factors are now explicitly reflected in the revised schematic and accompanying description [19–21].

Figure 2a illustrates the device structure of the tandem perovskite solar cell (TPSC), comprising five key layers: fluorine-doped tin oxide (FTO) serving as the front contact, C_{60} as the electron transport layer (ETL), $MASnI_3$ functioning as the perovskite absorber, MoO_3 acting as the hole transport layer (HTL), and crystalline silicon (C-Si) as the metal back contact. This configuration is specifically designed for a four-terminal (4T) tandem solar cell, where the top and bottom sub-cells are stacked sequentially. Figure 2b) presents the corresponding energy band diagram, highlighting proper band alignment between the active perovskite layer and the adjacent charge transport layers. In this setup, the FTO layer allows incident light to penetrate

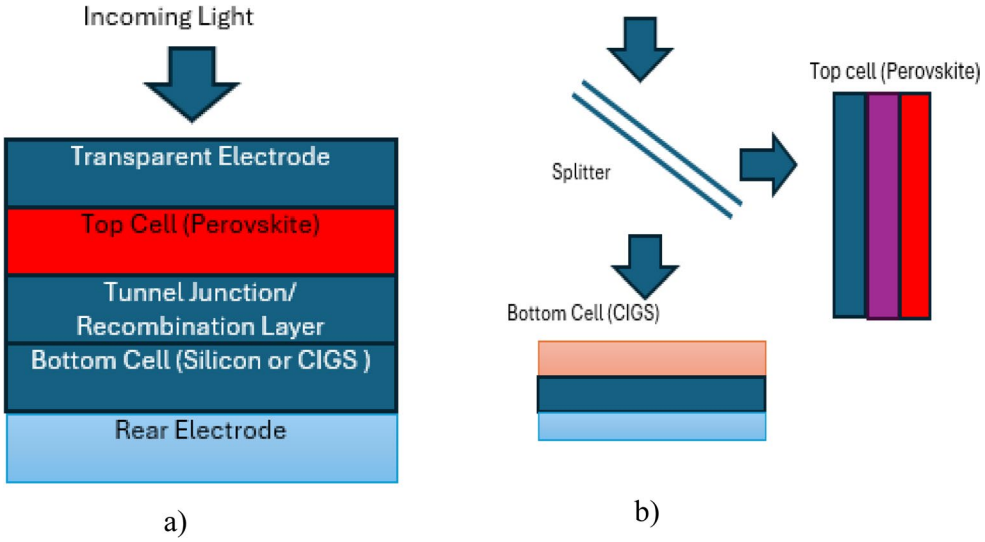

Fig. 1 Schematic diagrams of tandem solar cell architectures: **a)** monolithically integrated two-terminal (2T) structure featuring a series connection via a recombination layer for current matching; and **b)** optical spectrum splitting system that separates sunlight by wavelength

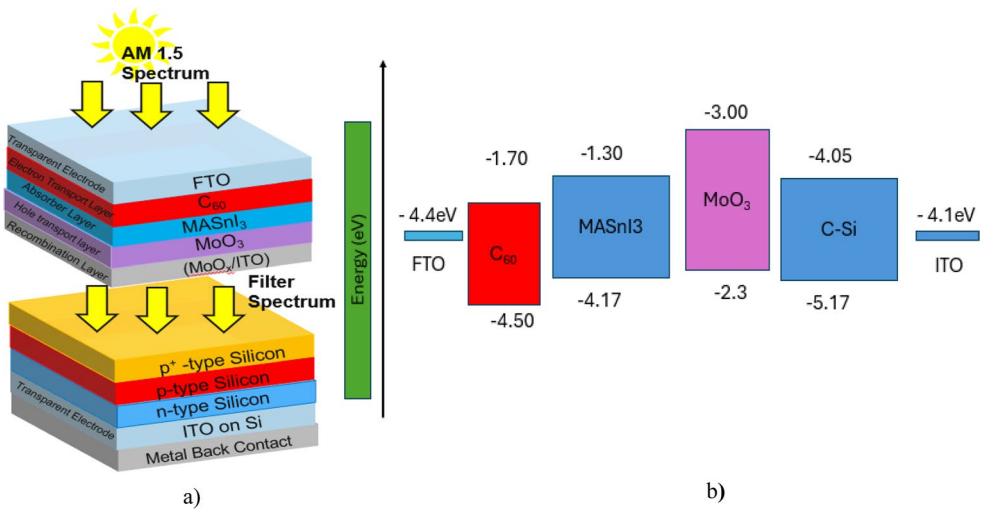

Fig. 2 **a** Schematic illustration of the tandem perovskite solar cell showing the top and bottom sub-cell layers; **b** corresponding energy level diagram depicting band alignment and charge transport pathways

to the underlying layers. The $MASnI_3$ perovskite absorbs photons to generate electron-hole pairs. The ETL facilitates the extraction and transport of electrons toward the front electrode, while the HTL directs holes to the back electrode, enabling efficient charge separation and collection.

The transparent electrode is defined as the front contact that enables optical transmission while maintaining lateral conductivity for the top perovskite sub-cell. This ensures efficient charge collection without impeding light absorption. The recombination layer is illustrated as an ohmic interconnect that facilitates carrier recombination and current continuity between the perovskite and silicon sub-cells, thereby supporting current matching across the two-terminal tandem stack [6–8]. We additionally describe process-aware constraints (e.g., sputter-induced damage in front electrodes and optimized ITO thickness in recombination layers) and reference established design strategies now reflected in our stack illustration and accompanying text [7, 8].

The transparent electrode, modeled as fluorine-doped tin oxide (FTO), serves as the front contact for the perovskite sub-cell, enabling high optical transmission while maintaining lateral conductivity for efficient charge collection [22–24].Positioned between the perovskite and silicon sub-cells, the recombination layer functions as an ohmic interconnect that facilitates carrier recombination electrons from the top cell and holes from the bottom cell ensuring current continuity and enabling current matching, which is critical for maximizing efficiency in 2 T tandem configurations [22–24]. In our simulation, this layer is represented by a MoO_3/ITO bilayer, selected for its favorable band alignment, high transparency, and ability to suppress interfacial recombination losses. To reflect process-aware constraints, we have added discussion on sputter-induced damage during ITO deposition and the importance of optimizing ITO thickness to balance conductivity and optical losses [23, 24].

2.2 Simulation parameters of MoO_3 and interfacing layers using SCAPS

In the simulated device structure, the hole transport layer (HTL) is represented by MoO_3, positioned adjacent to the perovskite absorber ($MASnI_3$) and followed by the electron transport layer (ETL), C_{60}. All material layers were defined accordingly in SCAPS-1D, with input parameters derived from previously reported experimental manuscripts [9, 15, 16, 25] with appropriate band alignment and efficient carrier extraction. Key properties include wide bandgap, high electron affinity, and matched energy level alignment between MoO_3 and $MASnI_3$ absorber layer to ensure an efficient hole transport pathway. The physical and electrical properties of MoO_3, such as doping concentration, thickness, and interface defect density. SCAPS-1D has been extensively employed to simulate the performance of lead-free perovskite solar cells, as it enables the optimization of critical parameters, including the hole transport layer (HTL) [17]. Table 1 provides a summary of the material parameters values applied in this simulation work. The layer thickness, MoO_3 doping, and interface defects on each layer were analyzed.

2.3 Layer input parameters in the silicon bottom cell

In the tandem solar cell configuration, three distinct silicon layers were defined in SCAPS-1D to form the full bottom-cell architecture, which are P^+Si, P-Si (optimized), and N-Si. The parameters for each silicon layer were set to reflect its doping type, electrical function, and role in carrier transport, based on previously reported for high-efficiency silicon solar cells. Table 2 shows the material parameters used for the silicon bottom cell as implemented in the SCAPS-1D simulation.

The doping concentrations (10^{10}–10^{19} cm^{-3}) and defect densities (10^{10}–10^{19} cm^{-2}) were selected to represent the reported physical behavior of MoO_3, $MASnI_3$, C_{60}, and crystalline silicon in tandem solar cells. These ranges encompass both intrinsic and extrinsic regimes, spanning from low-conductivity semiconductors to highly doped transport layers. For instance, MoO_3 as a hole transport layer typically exhibits p-type conductivity induced by oxygen vacancies, with doping levels in the 10^{16}–10^{19} cm^{-3} range depending on deposition conditions [26, 27]. Likewise, $MASnI_3$ is highly sensitive to defect states arising from Sn^{2+} oxidation and halide vacancies, which can introduce deep traps and strongly influence recombination dynamics.

Table 1 Basic Parameters for MoO_3 (HTL), $MASnI_3$ (Absorber Layer) and C_{60} (ETL) of the Top-Cell of PSC

Parameters/Materials	MoO_3[15]	$MASnI_3$[16]	C_{60} [16]
Thickness (μm)	Variable	Variable	Variable
Bandgap (ev)	3.750	1.300	1.700
Electron affinity (ev)	2.300	4.170	3.900
Dielectric permittivity (relative)	4.450	8.200	4.200
CB effective density of states ($1/cm^3$)	2.42×10^{19}	1×10^{18}	8×10^{19}
VB effective density of states ($1/cm^3$)	2.42×10^{19}	1×10^{18}	8×10^{19}
Electron thermal velocity (cm/s)	1×10^7	1×10^7	1×10^7
Hole thermal velocity (cm/s)	1×10^7	1×10^7	1×10^7
Electron mobility (cm^2/Vs)	1.1×10^3	1.6	2.17
Hole mobility (cm^2/Vs)	1.1×10^3	1.6	3.5×10^{-3}
Shallow uniform donor density N_D ($1/cm^3$)	0	0	2.6×10^{18}
Shallow uniform acceptor density N_A ($1/cm^3$)	Variable	1×10^{16}	0
Nt defect ($1/cm^3$)	Variable	Variable	Variable

Table 2 Parameters for the bottom cell of silicon solar cell

Parameters/Materials	P^+Si [19]	P Si (Optimize) [19]	N^-Si [19]
Thickness µm	0.200	Variable	0.550
Bandgap (ev)	1.120	1.120	1.120
Electron affinity (ev)	4.050	4.050	4.050
Dielectric permittivity (relative)	11.900	11.900	11.900
CB effective density of states (1/cm^3)	2.819×10^{19}	2.58×10^{19}	2.58×10^{19}
VB effective density of states (1/cm^3)	1.04×10^{19}	2.65×10^{19}	2.65×10^{19}
Electron thermal velocity (cm/s)	1×10^7	1×10^7	1×10^7
Hole thermal velocity (cm/s)	1×10^7	1×10^7	1×10^7
Electron mobility (cm²/Vs)	1.4×10^3	1350	45
Hole mobility (cm²/Vs)	4.5×10^2	450	47
Shallow uniform donor density ND (1/cm^3)	0	0	7×10^{20}
Shallow uniform acceptor density NA (1/cm^3)	1×10^{13}	Variable	0
Nt defect (1/cm^3)	1×10^{16}	Variable	0

Table 3 Parameter of defect density at interface layer

Parameters/Materials	C_{60}/$MASnI_3$	$MASnI_3$/MoO_3
Defect type	Neutral	Neutral
Electron capture cross section (cm^{-2})	1.0×10^{-19}	1.0×10^{-19}
Hole capture cross section (cm^{-2})	1.0×10^{-19}	1.0×10^{-19}
Energy Distribution	Single	Single
Energy level with respect to Ey	0.6	0.6
Characteristic energy (Ev)	-	-
Total density (cm^{-2})	Variable	Variable

The defect density range applied here allows simulation of both passivated interfaces and degraded conditions, consistent with experimental observations [27]. In addition, the selected ranges align with established SCAPS-1D modeling practices, where parameter sweeps are benchmarked against experimental single-junction references and tandem-relevant interfaces [7, 9]. This ensures that the parameter space captures realistic variability while enabling sensitivity analysis of transport and recombination pathways. Overall, this approach provides transparency in how material properties and defect densities influence device performance, while maintaining consistency with reported experimental data.

2.4 Study of interface defects near the MoO_3 hole transport layer

Alongside the simulation of material parameters, the impact of defects at the interfaces between adjacent layers was also assessed using SCAPS-1D. Key interfaces modeled include the MoO_3 hole transport layer (HTL)/$MASnI_3$ perovskite absorber interface and the C_{60} electron transport layer (ETL)/$MASnI_3$ interface. To evaluate the influence of interface recombination on tandem cell performance, a broad range of interface defect densities, from 1×10^{10} to 1×10^{19} cm^{-2}, was incorporated into the simulations. The essential parameters used for interface defect modeling are summarized in Table 3.

2.5 Fundamental Equations Governing SCAPS-1D Simulations

The simulation work was completely done using Solar Cell Capacitance Simulator (SCAPS-1D) software, a one-dimensional solar cell simulation program developed at ELIS, University of Gent. The output of the simulated device structure is computed using curves obtained from Poisson Eq. (1) and the continuity equations for electrons (2) and holes (3) under steady-state conditions as follows [14]. Equation (4) is utilized to transmit the spectrum by the top cell (PSC). Using this software, different types of solar cells were contqtad by systematically modifying up to five functional layers for which simulations were conducted under dark conditions and AM 1.5G 1 sun illumination. Primary parameters and properties of the device were varied and optimized for the perovskite solar cell.

Poisson Eq.

$$\begin{aligned} \frac{d\varnothing(x)}{dx} &= \frac{e}{\varepsilon\epsilon}(\rho(x) - n(x) + N_D - N_A + \rho_\rho \rho_n \\ g_D(E) &= G_{Md}\exp[-(E - E_{Pkd})/2_d \\ g_A(E) &= G_{Ma}exp[-(E - E_{Pka})^2/2_{a^2}] \end{aligned} \quad (1)$$

Where, $\varnothing(x)$= Electrostatic potential

e = Electric charge.

ε_o= Vacuum permittivity

ε_r= Relative permittivity.

p and n are the hole electron concentration.

N_D = Charged impurities of donor.

N_A = Charged impurities of acceptor.

$\rho_\rho$and ρ_n are holes and electron distribution.

The Drift and Distribution Equations are:

$$J_n = D_n \frac{dn}{dx} + \mu_n n \frac{d\varphi}{dx} \quad (2)$$

$$J_p = D_p \frac{dn}{dx} + \mu_p p \frac{d\varphi}{dx} \quad (3)$$

J_n = Electron current density.

D_n = Electron diffusion coefficient.

μ_n= Electron mobility.

J_p =Hole current density.

μ_p= Hole mobility.

Transmitted spectrum by top cell

$$S(\lambda) = S_0(\lambda).\exp\left(\sum_{i=1}^{4}\left(a_{materiali}(\lambda).d_{materiali}\right)\right) \quad (4)$$

3 Results and discussion

3.1 Effect of HTL layer thickness on device efficiency

The optimized thickness for the perovskite solar cell (PSC), tandem cell, and silicon sub-cells is depicted in Fig. 3a). The analysis was conducted over a thickness range of 10 nm to 100 nm. The data indicates a positive correlation between power conversion efficiency (PCE) and layer thickness. For both the PSC and tandem cells, a moderate increase in PCE is observed as thickness increases from 10 nm to 30 nm, corresponding to an improvement of approximately 2.64% (from 19.15% to 19.66%) and 1.78% (from 32.39% to 32.97%), respectively. Beyond 30 nm, up to 100 nm, the PCE values plateau and stabilize at approximately 19.70% and 33.03%, respectively. However, excessively thick hole transport layers (HTLs) can increase charge recombination probability due to longer carrier diffusion paths, ultimately reducing device efficiency [21]. Compared to silicon sub-cells, it has been demonstrated that as thickness increases, the consistency increases, reaching a maximum of 15.17% at 100 nm. This phenomenon arises from an increase in thickness, which improves the cell's ability to absorb photons, facilitating the production of a higher quantity of electron-hole pairs in the depletion zone. Thus, improving charge collecting efficiency and overall device performance [28].

3.2 Influence of doping concentration in HTL

Similar to the layer thickness investigations, doping concentration has affected PCE plots, as well. Figure 3b) illustrates the relationship between the doping concentration of the PSC, tandem structures, and silicon, along with their corresponding efficiencies. The data analyzed spans from 10^{10} to 10^{19}. The highest PCE attained in this domain is 34.19% for the tandem device, 20.48% for the PSC), and 15.72% for the silicon, all measured at a doping level of 10^{19} cm^{-3} [29]. The mobility of charge carriers remains relatively constant

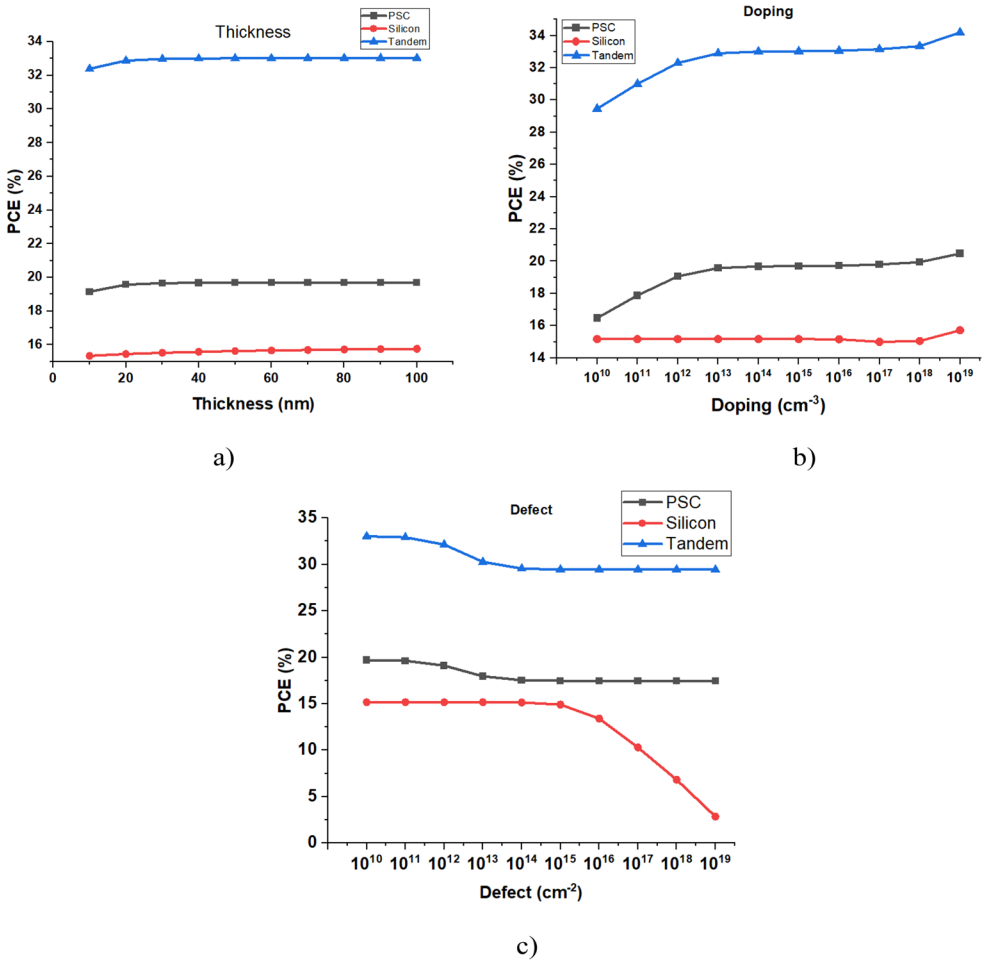

Fig. 3 Performance of PCE trends for tandem, PSC and silicon cells under optimized with (**a**) Various thickness, **b** Doping and **c** Total Interface defect density of MoO_3 as HTL in PSC

and stable within the doping range, even when influenced by photonic dispersion. However, increasing HTL doping elevates hole concentration and electrical conductivity, hence enhancing hole extraction from the perovskite layer and reducing recombination losses [30]. This improvement can be attributed to the inherent properties of MoO_3 as an effective HTL in this research work.

3.3 Total interface defect density (Nt) of MoO_3 on PSC and tandem layers

Figure 3(c) illustrates the efficiency and electrical properties of PSC, tandem, and silicon solar cells as a function of defect density, spanning values from 10^{10} to 10^{19} cm^{-2}. At the lowest defect density (10^{10} cm^{-2}), efficiencies reach 33.03% for the tandem device, 19.7% for the PSC, and 15.17% for the silicon sub-cell. Performance declines significantly once defect density exceeds 10^{15} cm^{-2}. Tandem cells are more sensitive to defects because of their multi-layer architecture, where each layer is essential for charge transport and light absorption. Defects in these layers increase carrier recombination at interfaces, impair charge extraction, and can induce bandgap mismatches that hinder charge separation and transport [4, 8, 31, 32]. As defect density rises, these issues accumulate more rapidly in tandem devices compared to single-layer cells, leading to a sharper drop in efficiency. High defect densities also shorten carrier lifetimes through enhanced scattering and recombination, while trapped charges at defective interfaces generate localized electric fields that drive ion migration and irreversible chemical processes [17].

3.4 Effect of interface defects on PSC performance

The maximum PCE of 19.7% was observed at 10^{10} cm^{-2} at the interface between C_{60} and $MASnI_3$ (ETL/absorber), as shown in Figure. 4a). As the defect density increases, a sharp decline in efficiency is recorded, reaching 3.16% at 10^{19} cm^{-2}. The degradation highlights that the presence of interface defects leads to the formation of trap states, which act as the recombination centers for the charge carriers. This results in reduced photocurrent and increased dark current, thereby decreasing device efficiency. This behavior is aligned with existing literature on the critical role of ETL/absorber in inverted PSC topologies [30, 33, 34].

The PCE decreases from 19.7% at 10^{10} to 17.54% at 10^{14} cm^{-2} and stabilizes at roughly 17.48% at 10^{19} cm^{-2}, as seen in Figure. 4b, at the $MASnI_3/MoO_3$ (absorber/HTL) interface. While a similar trend of efficiency degradation is observed, the drop is more gradual compared to the ETL/absorber interface. The presence of the Absorber/HTL (MoO_3) influences hole recombination, resulting in a reduced rate of PCE degradation, hence the durability of hole mobility and screening [35, 36]. This gradual decline suggests that MoO_3 (HTL) affects hole mobility. Due to their lower mobility and extended diffusion lengths compared to electrons, holes are less sensitive to defects. Furthermore, defects next to the valence band are less effective at capturing holes due to enhanced dielectric screening and shallower energy levels in $MASnI_3$, making it more challenging for defects in the vicinity of MoO_3 to contribute significantly to recombination. As a result, trap-assisted recombination

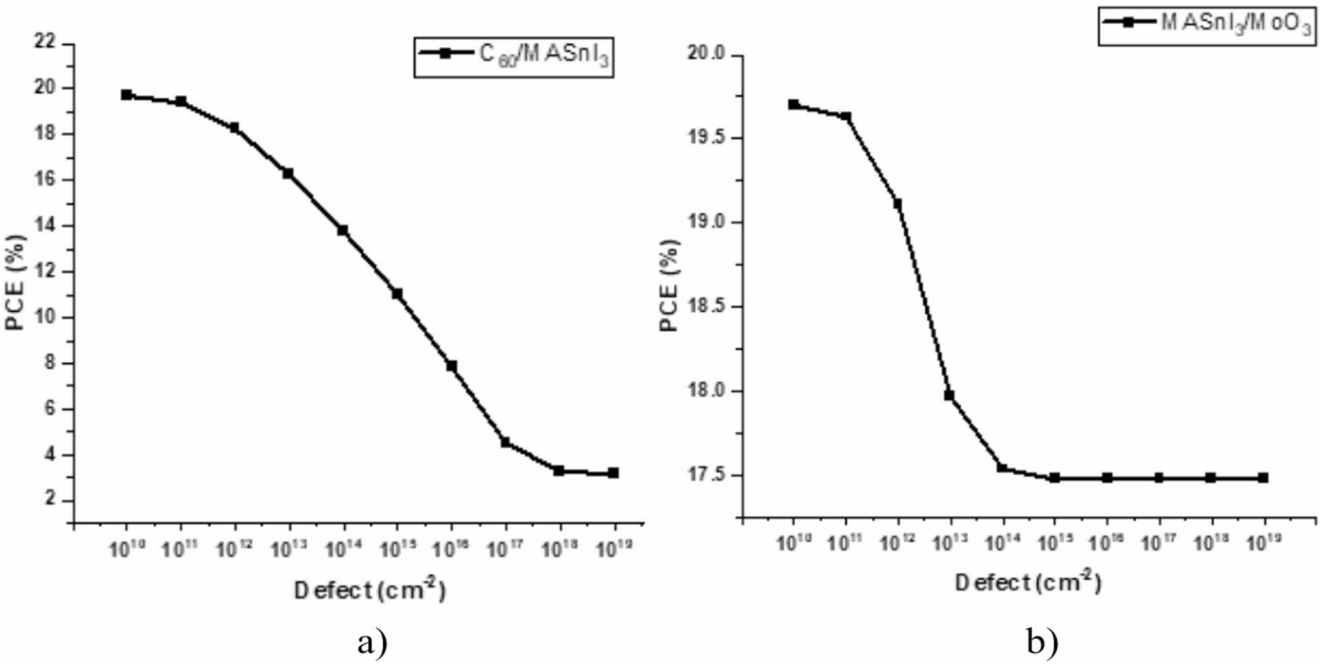

Fig. 4 Performance of interface defect density on PCE for (**a**) $C_{60}/MASnI_3$ (ETL/Absorber) and (**b**) $MASnI_3/MoO_3$ (Absorber/HTL) interfaces

is more moderate, and performance is efficiently sustained at higher defect densities [5, 6]. The vicinity of MoO_3 plays a key role in boosting the performance of perovskite solar cells by reducing the influence of defects that may exist at the interface between $MASnI_3$ (perovskite absorber) and MoO_3 (hole transport layer). MoO_3 mitigates trap-assisted recombination by stabilizing the interface, mostly owing to its dielectric screening effect, which diminishes the electric field surrounding defect sites. This inhibits defects from efficiently capturing charge carriers, especially holes, thus diminishing recombination and enhancing charge extraction. To minimize energy loss in reflective metal thin film electrodes, an extra dielectric layer, such as MoO_3, is utilized externally to the metal layer in the fabrication of ST devices for enhanced performance [37]. The presence of MoO_3 near the perovskite layer reduces recombination due to its dielectric characteristics and shallow energy levels, resulting in enhanced solar cell performance.

3.5 Effect of absorber doping on recombination rate

The recombination rate in the PSC is shown to be affected by the concentration of doping in Figure 5a). The doping concentration was varied from 1×10^{16} to 1×10^{19} $cm^{-3}$and the inset shows the entire graph. As doping concentration increases from 10^{16} to 10^{19} cm^{-3}, recombination rate significantly diminishes or deteriorates, particularly at 1×10^{19} cm^{-3}, where the lowest recombination is observed. This trend can be attributed to MoO_3 as HTL behavior, where excessive doping levels beyond 1×10^{18} cm^{-3} has been associated with reduced quantum efficiency due to the Moss-Burstein effect and defect-induced recombination [25] In a nutshell it possesses an excess of electrons obstructing the usual energy paths (Moss-Burstein effect), and there are material imperfections that result in energy dissipation rather than use (defect-induced recombination). Increasing the HTL(MoO_3) doping elevates hole concentration and conductivity, hence enhancing hole extraction from the perovskite layer [15]. This diminishes carrier accumulation at the HTL(MoO_3)/perovskite interface, hence decreasing interfacial recombination at a wavelength of 0.55 µm [15].

This trend indicates that increasing the doping concentration of the perovskite absorber layer ($MASnI_3$) from 1×10^{10} to 1×10^{19} cm^{-3} markedly reduced the number of traps within the bandgap due to enhanced band alignment and carrier selectivity. The enhancement in the material's carrier concentration leads to a decrease in the number of deep trap states, which in turn mitigates recombination losses. This doping modification improves the band alignment with the hole transport layer (HTL), like MoO_3, resulting in enhanced charge extraction and lower energy barriers at the interface. The enhancements lead to increased device efficiency, characterized by improved charge transport and minimized recombination in the $MASnI_3$-based perovskite solar cells, as evidenced by multiple simulation studies.

A higher doping concentration of $MASnI_3$ from 1×10^{10} to 1×10^{19} cm^{-3} improves the photovoltaic parameters - PCE, FF, Voc, and Jsc - of the solar cell, as shown in Fig. 5b). Specifically, PCE and FF increase from 16.48% to 19.58% and from 48.3 to 66.1, respectively 1×10^{10} to 1×10^{13} cm^{-3}. Subsequently, values remain relatively steady from 1×10^{14} to 1×10^{16} cm^{-3} with a PCE of 19.06% and FF of 66.4, before further increasing to maximum levels of PCE and FF of 20.48% and 67.51, respectively at 1×10^{19} cm^{-3}. The Voc also increases from 0.905 to 0.9718 V between 1×10^{10} and 1×10^{12}, remaining stable until doping reaches 1×10^{19}. The maximum open-circuit voltage attained is 0.9722 V at a density of 1×10^{19} cm^{-3}.

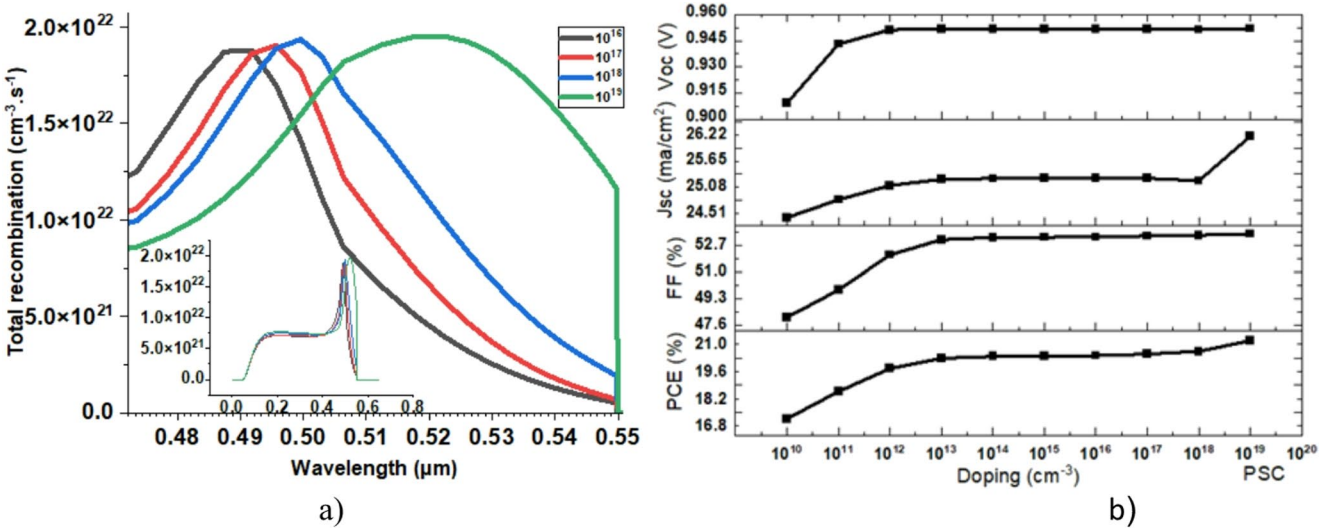

Fig. 5 Effect of Absorber Doping on (**a**) Inset Recombination rate and (**b**) Photovoltaic Performance of the PSC

The Jsc exhibits a tendency nearly identical to Voc, with an increase in doping between 1×10^{10} and 1×10^{13} cm^{-3} resulting in a rise in Jsc from 30.207 to 30.493 mA/cm^{-2}. The Jsc value remains constant at 30.510 mA/cm^{-2} from 1×10^{14} to 1×10^{18} cm^{-3}, with the maximum value of 31.204 mA/cm^{-2} attained at 1×10^{19} cm^{-3}.

The result suggested that increasing the doping concentration in the $MASnI_3$ absorber layer improves the photovoltaic parameters such as PCE, Voc, Jsc, and FF. However, excessive doping introduces additional recombination centers such as defects/impurities, which shorten carrier lifetimes and consequently elevate the recombination rate [26, 27, 38]. This confirms that doping in the $MASnI_3$ absorber layer influences the recombination, thereby improves performance. Optimal doping ensures the alignment of the energy band between the absorber and the HTL (MoO_3), promoting hole transport while limiting electron flow. MoO_3, when employed as an HTL, functions mainly as a selective contact for holes while forming a sufficient potential barrier for electrons, hence diminishing interfacial recombination at the anode/active layer interface. The findings affirm that absorber-layer technology is crucial in achieving high efficiency tandem solar cells [28].

3.6 Effect of $C_{60}/MASnI_3$ interface defect on recombination rate

The influence of the density of interface defects at the C_{60}/$MASnI_3$, junction is shown in Fig. 6a), with the total recombination rate profile displayed in the inset. As the defect density increases from 1×10^{10} to 1×10^{19} cm^{-2}, a significant rise in recombination is observed, indicating a high concentration of trap states within the perovskite bandgap. These trap states act as recombination centers—originating from defects or impurities which reduce carrier lifetimes and increase recombination rates, ultimately degrading the device's performance [26, 27]. As recombination intensifies with increasing interface defect density, the power conversion efficiency (PCE) declines sharply from its maximum value of 19.7% to 3.16%. Beyond a defect density of 1×10^{18} cm^{-2}, the PCE reaches a saturation point, maintaining a constant value of 3.16%, indicating severe recombination-limited performance in this regime.

The trend of a sharp decline in performance due to an increase in the density of interface defects is corroborated by Fig. 6b). As defect density rises from 1×10^{10} to 1×10^{19} cm^{-2}, the power conversion efficiency (PCE) drops sharply from a maximum of 19.7% to 3.16%, stabilizing at this lower value beyond 1×10^{18} cm^{-2}. A similar decline is observed in both open-circuit voltage (Voc) and short-circuit current density (Jsc). Voc decreases progressively from 0.9716 V at 1×10^{10} cm^{-2} to 0.3696 V at 1×10^{19} cm^{-2}. Jsc remains constant at 30.502 mA/cm^2 between 1×10^{10} and 1×10^{15} cm^{-2} but drops steadily to 16.25 mA/cm^2 as defect density increases beyond 1×10^{16} cm^{-2}. The fill factor (FF) shows a slight peak at 1×10^{12} cm^{-2}, followed by a gradual decline, reaching 52.63% at 1×10^{19} cm^{-2}. In SCAPS-1D simulations, carrier recombination at interfacial defect states is represented similarly to bulk defect recombination via carrier capture and emission processes dictated by Shockley–Read–Hall statistics. The interface recombination rate is calculated with the Pauwels–Vanhoutte formalism, an extension of the SRH theory utilized in SCAPS-1D [32–34]. Comparable methodologies have been utilized in recent investigations regarding interface faults in environmentally sustainable perovskite solar cells [35].

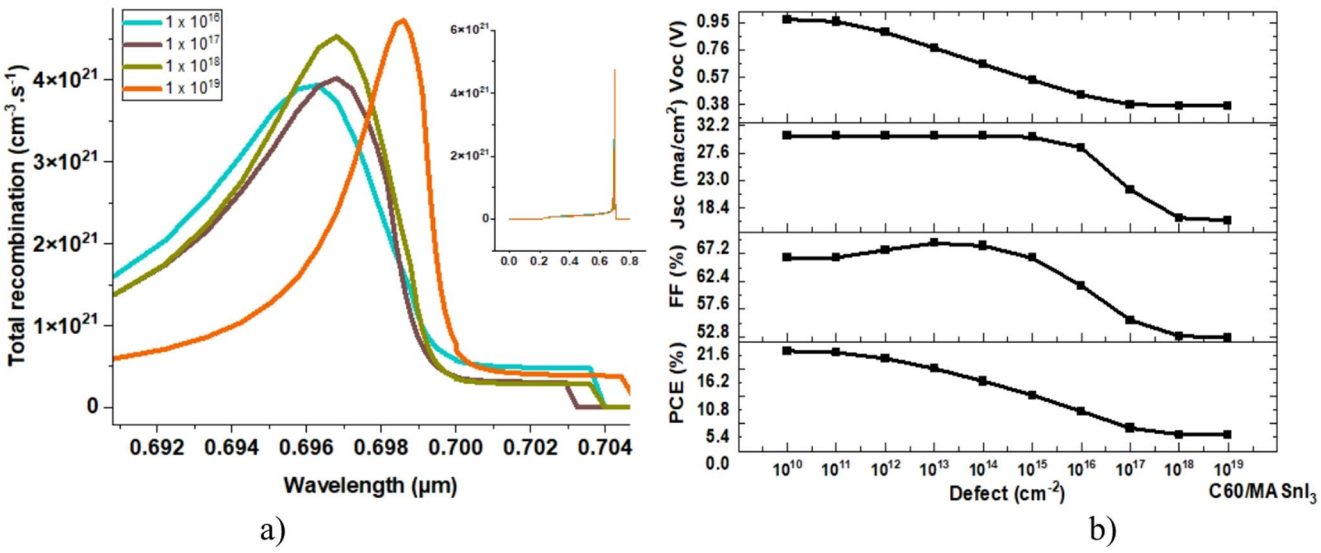

Fig. 6 Performance of interface defect $C_{60}/MASnI_3$ (**a**) Inset Recombination Rate and (**b**) Photovoltaic Performance in PSC

These losses are primarily due to enhanced recombination at defect sites, often located at grain boundaries or interfaces, which also facilitate moisture and oxygen ingress and result in accelerating perovskite degradation [30, 35]. For instance, Sn^{2+} oxidation at the C_{60} interface deteriorates $MASnI_3$, increasing recombination [30]. Overall, interface defects act as both recombination centers and degradation triggers but can be mitigated through careful interface engineering and passivation strategies to enhance both efficiency and stability.

At the MoO_3/$MASnI_3$ interface, oxygen atoms in MoO_3 can coordinate with under-coordinated Sn^{3+} and fill iodide vacancies, forming Sn–O–Mo bonds that reduce defect densities and stabilize Sn oxidation states. These interactions diminish trap states and suppress non-radiative recombination, thereby improving charge selectivity and open-circuit voltage [9, 26]. Concurrent iodide migration toward the interface may further neutralize traps, while redox transitions of Mo^{6+} to Mo^{5+} generate interfacial dipoles that facilitate band alignment, enhance hole extraction, and block electron backflow. Such mechanisms collectively strengthen charge collection and device performance.

At the MoO_3/$MASnI_3$ interface, oxygen atoms in MoO_3 can coordinate with under-coordinated Sn^{3+} and fill iodide vacancies, forming Sn–O–Mo bonds that reduce defect densities and stabilize Sn oxidation states. These interactions diminish trap states and suppress non-radiative recombination, thereby improving charge selectivity and open-circuit voltage [9, 26]. Concurrent iodide migration toward the interface may further neutralize traps, while redox transitions of Mo^{6+} to Mo^{5+} generate interfacial dipoles that facilitate band alignment, enhance hole extraction, and block electron backflow. While this bonding model is consistent with prior reports, direct contact between MoO_3 and halide perovskites may also introduce interfacial instability and degradation [34, 35]. To reflect this, our description of Mo–O–Sn bonding is presented as a hypothesis supported by literature and intended to guide experimental validation through XPS, UPS, and depth profiling [5, 39].

Beyond the bonding hypothesis, the multifunctional role of MoO_x at the ITO recombination layer can be explained through complementary chemical and physical passivation effects. Chemical passivation arises from interfacial bond formation, particularly Mo–O–Sn linkages, which neutralize under-coordinated tin sites and fill iodide vacancies, thereby lowering trap density, stabilizing Sn oxidation states, and mitigating defect-induced recombination losses [40, 41]. In contrast, physical passivation is governed by the intrinsic dielectric and energetic properties of MoO_x. Its high dielectric constant enables effective screening of interfacial electric fields, while its deep work function (6.7 eV) promotes favorable band alignment for hole extraction and electron blocking [26, 41]. These effects diminish recombination without altering absorber stoichiometry, providing electrostatic stabilization rather than chemical modification. Taken together, the MoO_x/ITO recombination layer simultaneously delivers chemical passivation through defect neutralization and physical passivation via dielectric screening and energy level alignment, consistent with synergistic bulk/interface passivation strategies reported in high-efficiency inverted perovskite devices and monolithic tandem architectures [42, 43] (Fig. 7).

3.7 J-V and EQE characteristics of tandem cell

Under current-matching conditions, Fig. 8a shows the simulated current-voltage (J-V) characteristics of the two-terminal tandem device, as well as the individual J-V curves for the top and bottom sub-cells. The results indicate that the top perovskite sub-cell acts as the current-limiting component of the tandem structure, which is expected due to its higher bandgap. This sub-cell also exhibits a relatively elevated open-circuit voltage (V_{OC}), a consequence of the wide-bandgap absorber material. The extracted photovoltaic parameters for the top, bottom, and tandem devices are summarized in Tables 2 and 3, confirming the effectiveness of the current-matching strategy and overall device optimization [30]. The simulated two-terminal perovskite/silicon tandem solar cell achieved a total power conversion efficiency (PCE) of 34.19%, with individual contributions from the top and bottom sub-cells of 20.48% and 15.72%, respectively. These values reflect an optimized device architecture with efficient charge extraction and minimized recombination losses across both junctions Each sub-cell's unique spectrum contribution is shown in Fig. 8b), which displays the tandem structure's external quantum efficiency (EQE) spectra. The top perovskite cell efficiently absorbs and converts high-energy photons in the short-wavelength range, while the bottom silicon cell captures the longer-wavelength photons transmitted through the top layer. The combined EQE profile demonstrates effective utilization of a broad portion of the solar spectrum, confirming the spectral complementarity between the two sub-cells.

These simulation results highlight the potential of optimized tandem architectures to exceed the performance of conventional single-junction devices. The findings also suggest that with further interface engineering and material optimization, efficiencies beyond current experimental benchmarks are attainable, bringing the technology closer to commercial feasibility [13] (Table 4).

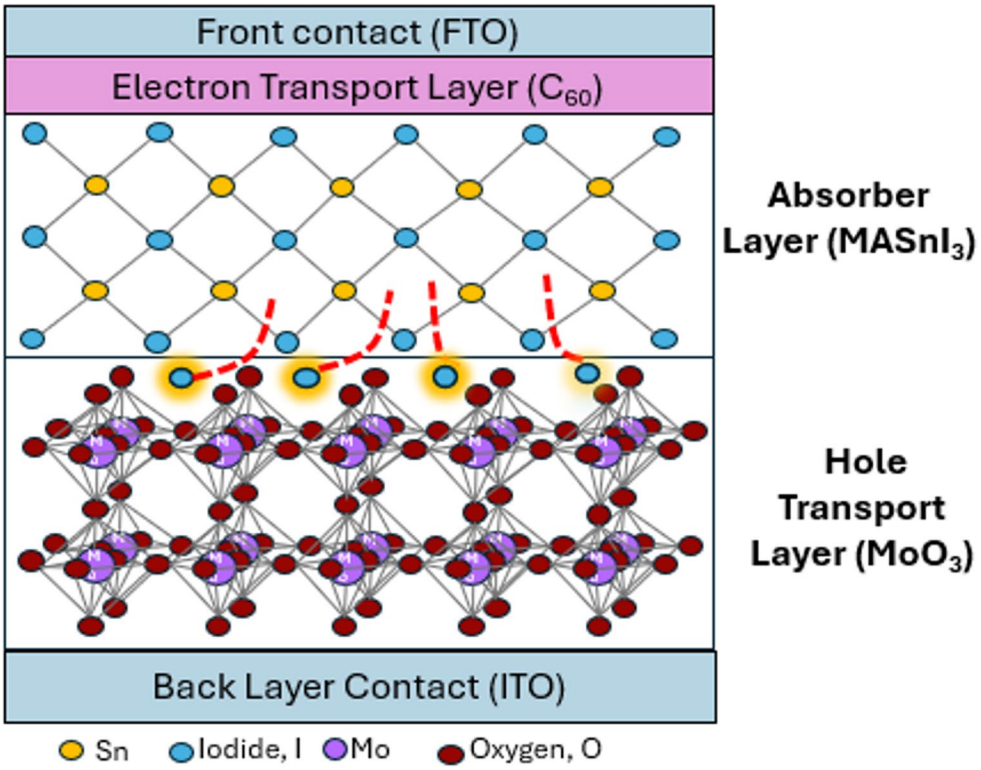

Fig. 7 The passivation interaction by the MoO_3 (HTL) within the $MASnI_3$ (Absorber layer) grain interfaces to minimize the charge recombination

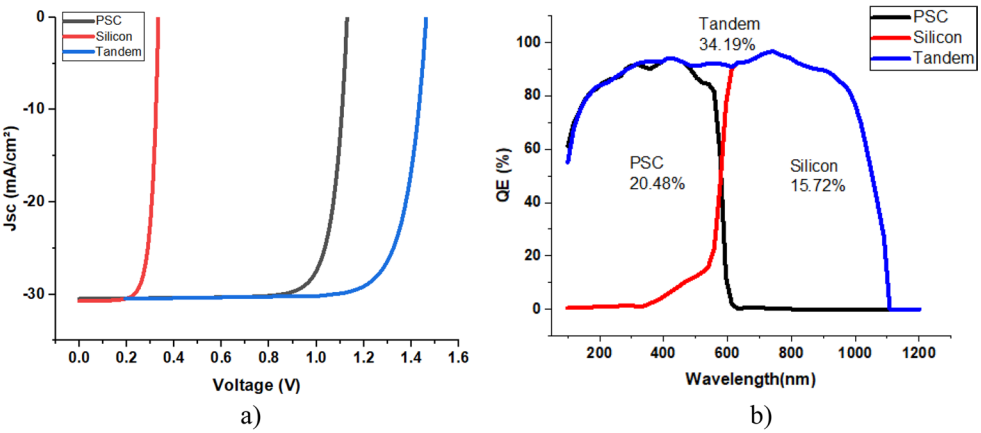

Fig. 8 **a** Variation of J-V curve of the standalone PSC, Silicone and tandem cell. **b** EQE of standalone PSC, Silicon and tandem cell

Table 4 Photovoltaic performance of the standalone PSC and tandem solar cell

Experimental Work MoO_3 [15]	Cell	Voc(V)	Jsc(mA/cm^2)	FF(%)	PCE(%)
	Single Cell	0.95	22.58	82.56	17.82
Top Cell MoO_3 (PSC) (Our Work)	Single cell	0.9722	31.204	67.51	20.48
Experimental Work [44]	Tandem Cell (PSC-PSC-Organic)	3.26	10.67	0.82	25.2%
Experimental Work [13]	Tandem Cell (PSC-PSC)	2.047	18.30	86.23	32.30%
Tandem Cell (Our Work)	Tandem Cell (PSC- Si)	1.4937	33.04	69.288	34.194%

3.8 Simulated vs. experimental efficiency gap

The simulated PCE of 34.19% does not correspond to a single-junction perovskite device but rather to a two-terminal (2T) monolithic perovskite/silicon tandem architecture. The Shockley Queisser limit constrains single-junction solar cells to 30–33% under AM1.5G illumination [45], whereas tandem architectures surpass this limit by splitting the solar spectrum between two absorbers, thereby reducing thermalization losses and enhancing photocurrent. Detailed balance

calculations predict efficiency limits of 40–45% for optimized perovskite/silicon 2 T tandems [46, 47], and the simulated value of 34.19% represents an optimistic yet physically reasonable upper bound within this framework. The difference between simulated and reported experimental values arises because real devices suffer from non-idealities such as interfacial defects, Sn oxidation, parasitic absorption, and scalability challenges, which reduce practical efficiencies to 15–20% for Sn-based perovskites. Bridging this gap requires process-aware strategies including improved interface passivation, optimized recombination layer thickness, and transparent electrode engineering. Specifically, mitigation of interfacial sputter damage during electrode deposition [27], careful tuning of recombination layer thickness to balance transport and optical losses [48], and improved transparent electrode design to minimize parasitic absorption [27, 48] are critical pathways. Benchmarking against experimental single-junction baselines and tandem demonstrations will be essential to validate simulation predictions and guide pathways toward experimental realization.

While SCAPS-1D remains a widely adopted tool for exploring carrier transport and recombination dynamics in perovskite solar cells, its simulated results must be interpreted within the framework of inherent limitations. The model is based on a one-dimensional drift–diffusion formalism with steady-state solutions, which assumes uniform carrier flow perpendicular to the device plane and neglects lateral inhomogeneities such as grain boundaries, pinholes, or shunting paths that are common in real thin-film devices. Interfaces are treated as abrupt and defect-free junctions, while the absorber is assumed to possess uniform composition and stoichiometry. Importantly, SCAPS-1D omits dynamic processes such as ion migration, defect drift, light soaking, and chemical degradation, all of which are known to strongly influence hysteresis, stability, and long-term performance in perovskite systems [31, 49]. These simplifications suppress non-radiative recombination channels and yield optimistic values of open-circuit voltage, fill factor, and overall PCE compared to experimental devices, positioning the simulated efficiency as an upper bound rather than a direct surrogate. Despite these constraints, SCAPS-1D remains valuable for sensitivity analysis and comparative benchmarking, as it enables systematic evaluation of how band alignment, defect density, and layer thickness influence device physics. Our parameter choices were aligned with best practices referencing experimental single-junction and tandem configurations [15, 23]. Nevertheless, acknowledging these limitations highlights the importance of validating simulated predictions through process-aware experimental strategies, including careful control of interfacial quality, benchmarking against single-junction baselines, and integration into tandem demonstrations. In this context, SCAPS-1D serves as a comparative guide for optimization rather than a substitute for real device data.

4 Conclusion

This study highlights the effectiveness of a tailored molybdenum trioxide (MoO_3) hole transport layer (HTL) in enhancing the efficiency and stability of lead-free perovskite/silicon tandem solar cells. Through SCAPS-1D simulations, parameters such as HTL thickness, doping concentration, and interface defect density were systematically analyzed, yielding an optimized configuration with a simulated power conversion efficiency (PCE) of 34.19%. This high efficiency is attributed to improved charge extraction and reduced interfacial recombination losses enabled by Mo–O–Sn bonding at the MoO_3/$MASnI_3$ interface, surpassing the individual efficiencies of the perovskite (20.48%) and silicon (15.72%) sub-cells under AM 1.5G illumination. A key finding is the strong dependence of tandem performance on interface defect density, where controlled defect levels mitigate non-radiative recombination and preserve voltage and current output.

Beyond confirming MoO_3 as both a robust hole transport material and an interfacial stabilizer, this work establishes a theoretical foundation for experimental validation. Future research should focus on translating these simulation results into practical fabrication by optimizing MoO_3 deposition methods (e.g., thermal evaporation, sputtering) to minimize interfacial damage, controlling oxygen stoichiometry to stabilize Mo oxidation states, and employing advanced characterization techniques such as XPS, UPS, and depth profiling to probe Mo–O–Sn bonding and defect passivation. Additionally, scaling strategies including large-area uniformity, tandem integration, and stability testing under operational stress will be critical to bridge the gap between simulated and experimental efficiencies. These steps will advance sustainable, high-performance, lead-free tandem photovoltaics from theoretical promise toward practical realization.

Acknowledgements This work was funded by the Royal Society of Chemistry, UK, under grant R24-4991922226, and registered at Universiti Teknikal Malaysia, Melaka, under grant no. ANTARABANGSA/RSC/2024/FTKEK/A00074.

Author contributions The manuscript was written through the contributions of all authors. All authors have approved the final version of the manuscript. All authors contributed to the Conceptualization. **Zulfanizam Abdul Wahab**: Investigation, formal analysis, writing and original draft. **Nabilah Ahmad Jalaludin**, **Nur Aliesa Johari** and **Mazlin Aida Mohamood**: Visualization, data curation. **Ahmad Nizammudin Mustafa**, **Fauziyah Salehuddin** and **Mohammad Aminul Islam**: validation. **F. Arith**: Project administration, methodology, writing, reviewing & editing and supervision.

Funding Open access funding provided by The Ministry of Higher Education Malaysia and Universiti Teknikal Malaysia Melaka. This work was funded by the Royal Society of Chemistry, UK under grant R24-4991922226, registered in Universiti Teknikal Malaysia, Melaka under grant no: ANTARABANGSA/RSC/2024/FTKEK/A00074.

Data availability The authors confirm that the data supporting the findings of this study are available within the article. Raw data that support the findings of this study are available from the corresponding author upon reasonable request.

Declarations

Competing interest On behalf of all authors, the corresponding author states that there is no conflict of interest.

References

1. O.V. Aliyaselvam et al., Unveiling the prospect of copper iodide as hole transporting layer in perovskite solar cell by selective dopant strategy: A review, Oct. 01, 2025, *Elsevier Ltd*. https://doi.org/10.1016/j.mssp.2025.109679
2. W.E. McMahon, J.F. Geisz, J. Buencuerpo, E.L. Warren, A framework for comparing the energy production of photovoltaic modules using 2-, 3-, and 4-terminal tandem cells. Sustain. Energy Fuels **7**(2), 461–470 (2022). https://doi.org/10.1039/d2se01167k
3. K. Alberi et al., A roadmap for tandem photovoltaics, Mar. 20, 2024, *Cell Press*. https://doi.org/10.1016/j.joule.2024.01.017
4. a B. Xin Wu, Li, *a,d Zonglong Zhu, Chu-Chen Chueh*c, and b,d,e Alex. K.-Y. Jen*a, Designs from Single Junction, Heterojunction to Multijunction for High-Performance Perovskite Solar Cells, in *AIChE Annual Meeting, Conference Proceedings*, American Institute of Chemical Engineers, 2019. https://doi.org/10.1039/x0xx00000x
5. R. Ukai, Y. Wasai, Y. Izumi, H. Shirai, Solution-Processed Monolithic Tandem Perovskite/n-Si Hybrid Solar Cells Using MoO3/InZnO Bilayer-Based Interconnecting and Window Layers. Cryst. (Basel). **14**(1) (Jan. 2024). https://doi.org/10.3390/cryst14010068
6. J. Liu, X. Yin, Y. Guo, M. Que, W. Que, The diverse passivation effects of fullerene derivative on hysteresis behavior for normal and inverted perovskite solar cells. J. Power Sources (2020). https://doi.org/10.1016/j.jpowsour.2020.228156
7. Y.N. Jusoh et al., Formulation of Nb-doped ZnO nanoparticles towards improved photo conversion performance via luminescent down-shifting of the incident spectrum. Int. J. Renew. Energy Dev. **14**(3), 441–449 (May 2025). https://doi.org/10.61435/ijred.2025.60983
8. N.A. Jalaludin et al., Efficient hole extraction by doped-polyaniline/graphene oxide in lead-free perovskite solar cell: a computational study. Phys. Scr. **100**(2) (Feb. 2025). https://doi.org/10.1088/1402-4896/ada4e8
9. M.A. Islam et al., Spin-coated high mobility MoO3 thin film for designing highly efficient lead-free perovskite solar cells. Ceram. Int. **50**(13), 23847–23854 (Jul. 2024). https://doi.org/10.1016/j.ceramint.2024.04.111
10. G. Jia et al., Electron transport layer materials of perovskite solar cells, May 01, 2025, *Springer*. https://doi.org/10.1007/s10853-025-10883-w
11. A.A. Said et al., Sublimed C60 for efficient and repeatable perovskite-based solar cells. Nat. Commun. **15**(1) (Dec. 2024). https://doi.org/10.1038/s41467-024-44974-0
12. S. You et al., C60-based ionic salt electron shuttle for high-performance inverted perovskite solar modules. Science **388**(6750), 964–968 (2025). https://doi.org/10.1126/science.adv4701
13. G. Shankar, P. Kumar, B. Pradhan, All-perovskite two-terminal tandem solar cell with 32.3% efficiency by numerical simulation. Mater. Today Sustain. (2022). https://doi.org/10.1016/j.mtsust.2022.100241
14. S.S. Parui, A. Jariwala, V. Krishnapressad, R.R. Babu, V. Kheraj, Numerical And Experimental Insight On Lead Free MASnI3 Based Perovskite Solar Cell. J. Opt. (India). (2025). https://doi.org/10.1007/s12596-024-02374-z
15. F. Ali et al., Prospects of e-beam evaporated molybdenum oxide as a hole transport layer for perovskite solar cells. J. Appl. Phys. (2017). https://doi.org/10.1063/1.4996784
16. M. Mehrabian, E.N. Afshar, O. Akhavan, TiO2 and C60 transport nanolayers in optimized Pb-free CH3NH3SnI3-based perovskite solar cells. Mater. Sci. Eng. B Solid-State Mater. Adv. Technol. (2023). https://doi.org/10.1016/j.mseb.2022.116146
17. S. Banik, A. Das, B.K. Das, N. Islam, Numerical simulation and performance optimization of a lead-free inorganic perovskite solar cell using SCAPS-1D. Heliyon (2024). https://doi.org/10.1016/j.heliyon.2024.e23985
18. J. Madan, R. Shivani, Pandey, R. Sharma, Device simulation of 17.3% efficient lead-free all-perovskite tandem solar cell, *Solar Energy*, vol. 197, no. January, pp. 212–221, 2020, https://doi.org/10.1016/j.solener.2020.01.006
19. S. Sarker et al., A SCAPS simulation investigation of non-toxic MAGeI3-on-Si tandem solar device utilizing monolithically integrated (2-T) and mechanically stacked (4-T) configurations. Solar Energy **225**, 471–485 (2021). https://doi.org/10.1016/j.solener.2021.07.057
20. N.S. Noorasid et al., Improved performance of lead-free Perovskite solar cell incorporated with TiO 2 ETL and CuI HTL using SCAPs. Appl. Phys. Mater. Sci. Process. **129**(2) (Feb. 2023). https://doi.org/10.1007/s00339-022-06356-5
21. A.Y. Firhat, F. Arith, N.S. Noorasid, A. Nizamuddin Mustafa, A. Syahiman, M. Shah, SCAPS Numerical Analysis of Solid-State Dye-Sensitized Solar Cell Utilizing Copper (I) Iodide as Hole Transport Layer, https://doi.org/10.4186/ej.2009.VOL.ISSUE.pp
22. M. Härtel et al., Reducing sputter damage-induced recombination losses during deposition of the transparent front-electrode for monolithic perovskite/silicon tandem solar cells. Sol. Energy Mater. Sol. Cells. **252** (Apr. 2023). https://doi.org/10.1016/j.solmat.2023.112180
23. H.H. Park, Transparent electrode techniques for semitransparent and tandem perovskite solar cells. Electron. Mater. Lett. (1) (2021). https://doi.org/10.1007/s13391-020-00259-4
24. Ö, Ş. Kabaklı et al., Thickness Optimization of Front and Recombination ITO in Monolithic Perovskite/Silicon Tandem Solar

Cells. Solar RRL. **8**(20) (Oct. 2024). https://doi.org/10.1002/solr.202400454
25. Z. Abdul, N. Ahmad, M. Khanapiah, A. Nizamuddin, M. Mustafa, Insights of MoO3 HTL in Perovskite Solar Cells from a Simulation Perspective, pp. 31–38
26. M.A. Belbachir, A.Z. Djennati, S. Kerai, M. Khaouani, H. Rouigueb, Simulation validation and performance optimization of tandem perovskite/silicon solar cells based on experimental single-junction perovskite solar cell. J. Electron. Mater. **54**(10), 8618–8627 (2025). https://doi.org/10.1007/s11664-025-12173-2
27. G. Cao, X. Gu, J. Su, Z. He, B. Tang, Boosting the efficiency of lead-free MASnI3 perovskite solar cells through a bilayer CIGS structure approximating a gradient bandgap distribution. J. Mater. Chem. A (2025). https://doi.org/10.1039/d5ta01267h
28. U. Mandadapu, S.V. Vedanayakam, K. Thyagarajan, Simulation and analysis of lead based perovskite solar cell using SCAPS-1D. Indian J. Sci. Technol. **10**(11), 1–8 (2017). https://doi.org/10.17485/ijst/2017/v10i11/110721
29. V.H.D. Araújo, A.F. Nogueira, J.C. Tristão, L.J. dos Santos, Advances in lead-free perovskite solar cell design via SCAPS-1D simulations. RSC Sustain. (2025). https://doi.org/10.1039/d5su00526d
30. F. Wang, S. Bai, W. Tress, A. Hagfeldt, F. Gao, Defects engineering for high-performance perovskite solar cells. Dec. 01 2018 Nature Research https://doi.org/10.1038/s41528-018-0035-z
31. H. Lee, D. Li, Surface passivation to improve the performance of perovskite solar cells. Energies (2024). https://doi.org/10.3390/en17215282
32. H.J. Pauwels, G. Vanhoutte, The influence of interface states and energy barriers on the efficiency of heterojunction solar cells, 1978. https://doi.org/10.1088/0022-3727/11/5/009
33. K. Afridi, M. Noman, S.T. Jan, Evaluating the influence of novel charge transport materials on the photovoltaic properties of MASnI3solar cells through SCAPS-1D modelling. R. Soc. Open Sci. (2024). https://doi.org/10.1098/rsos.231202
34. M. Ismail, M. Noman, S.T. Jan, M. Imran, Boosting efficiency of eco-friendly perovskite solar cell through optimization of novel charge transport layers. R. Soc. Open Sci. (2023). https://doi.org/10.1098/rsos.230331
35. M.M. Haque et al., Study on the interface defects of eco-friendly perovskite solar cells. Solar Energy **247**, 96–108 (2022). https://doi.org/10.1016/j.solener.2022.10.024
36. I. Mosquera-Lois, Y.-T. Huang, H. Lohan, J. Ye, A. Walsh, R.L.Z. Hoye, Multifaceted nature of defect tolerance in halide perovskites and emerging semiconductors. Nat. Rev. Chem. (2025). https://doi.org/10.1038/s41570-025-00702-w
37. M.B. Upama et al., Low-temperature processed efficient and colourful semitransparent perovskite solar cells for building integration and tandem applications. Org. Electron. **65**, 401–411 (2019). https://doi.org/10.1016/j.orgel.2018.11.037
38. E. Gaubas, J. Vanhellemont, E. Simoen, I. Romandic, W. Geens, P. Clauws, Carrier lifetime dependence on doping, metal implants and excitation density in Ge and Si. Phys. B Condens. Matter **401–402**, 222–225 (2007). https://doi.org/10.1016/j.physb.2007.08.151
39. A.K. Chaudhary, S. Verma, R.K. Chauhan, MASnI3-based perovskite solar cell utilizing oxygen-free charge transport layers to alleviate Sn oxidation for stability: a comprehensive investigation. J. Renew. Sustain. Energy (2024). https://doi.org/10.1063/5.0220018
40. M. Burgelman, P. Nollet, S. Degrave, Modelling polycrystalline semiconductor solar cells. Thin Solid Films (2000). https://doi.org/10.1016/S0040-6090(99)00825-1
41. A. Sharma, A. Sharma, M. Garg, N. Kumar, S.K. Sharma, A.K. Sharma, Material and Interface Innovations in Perovskite–Silicon Tandem Solar Cells for Enhanced Stability and Efficiency, 2025, *Springer*. https://doi.org/10.1007/s11664-025-12581-4
42. M.R. Barget, M. Virgilio, G. Capellini, Y. Yamamoto, T. Schroeder, The impact of donors on recombination mechanisms in heavily doped Ge/Si layers. J. Appl. Phys. (2017). https://doi.org/10.1063/1.4986236
43. D. Soro et al., Modeling and simulation of an organic photovoltaic cell: ITO/MoO3/CARAPA/PCBM/Alq3/Al with SCAPS. Modeling and Numerical Simulation of Material Science **14**(03), 79–96 (2024). https://doi.org/10.4236/mnsms.2024.143005
44. K. Hussain, A. Gagliardi, Modelling tandem/multi-junction hybrid perovskite–organic solar cells: a combined drift–diffusion and kinetic Monte Carlo study. Solar Energy **243**, 193–202 (2022). https://doi.org/10.1016/j.solener.2022.07.033
45. Z. Li and B. Wei, "Surpassing Shockley–Queisser Efficiency Limit in Photovoltaic Cells," Dec. 01, 2025, Springer Science and Business Media B.V. https://doi.org/10.1007/s40820-025-01844-8
46. V. Neder, S. W. Tabernig, and A. Polman, "Detailed-balance efficiency limits of two-terminal perovskite/silicon tandem solar cells with planar and Lambertian spectral splitters."
47. A. Fell et al., "Elucidating the efficiency limit of silicon-based monolithic tandem cells through the combination of Auger and Shockley–Queisser limits," EES Solar, 2025, https://doi.org/10.1039/d5el00085h
48. H. Huang, Interface passivation strategies for high-performance perovskite solar cells using two-dimensional perovskites. Mater. Chem. Front. (2024). https://doi.org/10.1039/d4qm00560k
49. O.J. Allen, J. Kang, S. Qian, J.J. Hinsch, L. Zhang, Y. Wang, A theoretical review of passivation technologies in perovskite solar cells. Energy Mater. **4**(3) (2024). https://doi.org/10.20517/energymater.2023.111